J. Fluid Mech. (2019), *vol.* 874, *pp.* 797–820. © Cambridge University Press 2019
doi:10.1017/jfm.2019.468

Predictions of the effective slip length and drag reduction with a lubricated micro-groove surface in a turbulent channel flow

Jaehee Chang[1], Taeyong Jung[1,‡], Haecheon Choi[1,2,†] and John Kim[3]

[1]Department of Mechanical and Aerospace Engineering, Seoul National University, Seoul 08826, Korea

[2]Institute of Advanced Machines and Design, Seoul National University, Seoul 08826, Korea

[3]Department of Mechanical and Aerospace Engineering, University of California, Los Angeles, CA 90095, USA

(Received 6 January 2019; revised 2 June 2019; accepted 6 June 2019;
first published online 12 July 2019)

We perform direct numerical simulations of a turbulent channel flow with a lubricated micro-grooved surface to investigate the effects of this surface on the slip characteristics at the interface and the friction drag. The interface between water and lubricant is assumed to be flat, i.e. the surface-tension effect is neglected. The solid substrate, where a lubricant is infused, is composed of straight longitudinal grooves. The flow rate of water inside the channel is maintained constant, and a lubricant layer under the interface is shear driven by the turbulent water flow above. A turbulent channel flow with a superhydrophobic (i.e. air-lubricated) surface having the same solid substrate configuration is also simulated for comparison. The results show that the drag reduction with the liquid-infused surface highly depends on the lubricant viscosity as well as the groove width and aspect ratio. The amounts of drag reduction with the liquid-infused surfaces are not as good as those with superhydrophobic surfaces, but are still meaningfully large. For instance, the maximum drag reduction by the heptane-infused surface is approximately 13 % for a rectangular groove whose spanwise width and depth in wall units are 12 and 14.4, respectively, whereas a superhydrophobic surface with the same geometry results in a drag reduction of 21 %. The mean slip length normalized by the viscosity ratio and groove depth depends on the groove aspect ratio. The ratio of fluctuating spanwise slip length to the streamwise one is between 0.25 (ideal surface without groove structures) and 1 (i.e. isotropic slip), indicating that the slip is anisotropic. Using the Stokes flow assumption, the effective streamwise and spanwise slip lengths are expressed as a function of groove geometric parameters and lubricant viscosity. We also suggest a predictive model for drag reduction with the heptane-lubricated surface by combining the predicted effective slip lengths with the drag reduction formula used for riblets (Luchini *et al.*, *J. Fluid Mech.*, vol. 228, 1991, pp. 87–109). The predicted drag reductions are in good agreements with those from the present and previous direct numerical simulations.

Key words: drag reduction, turbulence control, turbulent boundary layers

†Email address for correspondence: choi@snu.ac.kr

‡Present address: LG Electronics, 51, Gasan digital 1-ro, Geumcheon-gu, Seoul, Korea

1. Introduction

Friction drag reduction in turbulent boundary layers has been investigated by many researchers owing to both its academic interest and economic benefits. Recently, superhydrophobic surface (SHS) has received much attention as a possible method for friction drag reduction, and many studies on laminar and turbulent flows over SHSs have been conducted both experimentally and numerically (see the reviews by Rothstein (2010), Golovin *et al.* (2016)). The main reason for drag reduction by SHS is known to be the slip occurring at the originally no-slip surface. This slip effect can be quantified as the effective slip length, and its analytical solutions have been derived as a function of the surface geometric parameters and viscosity ratio between the working fluid and air (Lauga & Stone 2003; Ybert *et al.* 2007; Belyaev & Vinogradova 2010; Schönecker, Baier & Hardt 2014; Li, Alame & Mahesh 2017).

For turbulent flows over SHSs, both numerical (Min & Kim 2004; Fukagata, Kasagi & Koumoutsakos 2006; Martell, Perot & Rothstein 2009; Busse & Sandham 2012; Park, Park & Kim 2013; Jelly, Jung & Zaki 2014; Türk *et al.* 2014; Lee, Jelly & Zaki 2015; Jung, Choi & Kim 2016) and experimental (Henoch *et al.* 2006; Daniello, Waterhouse & Rothstein 2009; Woolford *et al.* 2009; Jung & Bhushan 2010; Bidkar *et al.* 2014; Park, Sun & Kim 2014) results confirmed the drag reduction capability of SHS. Numerical studies have been conducted either by prescribing a constant slip length at the flat air–water interface (Min & Kim 2004; Fukagata *et al.* 2006; Busse & Sandham 2012), or by imposing the shear-free boundary condition at the air–water interface without considering flow in the air layer (Martell *et al.* 2009; Martell, Rothstein & Perot 2010; Park *et al.* 2013; Jelly *et al.* 2014; Türk *et al.* 2014; Lee *et al.* 2015; Rastegari & Akhavan 2015; Seo, García-Mayoral & Mani 2015; Seo & Mani 2016). Recently, Jung *et al.* (2016) indicated that the shear-free condition at the interface provides an over-estimated drag reduction by SHS. Most recently, Seo, García-Mayoral & Mani (2018) investigated the dynamic behaviour of the shear-free interface by considering the deformation of the interface through coupling the Young–Laplace equation with the flow, and suggested a threshold criterion for the failure of SHS. Some experimental studies of turbulent flows over SHS provided no significant drag reduction or even drag increase (Peguero & Breuer 2009; Greidanus, Delfos & Westerweel 2011; Aljallis *et al.* 2013), and these results were attributed to the air–water interface deformation, error in the drag measurement or air loss in the SHS structures (Park *et al.* 2014; Ling *et al.* 2016).

Previous experiments indicated that the air–water interface is prone to failure under pressure fluctuations and physical stresses (Aljallis *et al.* 2013; Park *et al.* 2014; Rosenberg *et al.* 2016). In this regard, a new surface structure called SLIPS (slippery liquid-infused porous surface) or LIS (liquid-impregnated surface or liquid-infused surface) has been considered as an alternative for drag reduction, as one can expect slip at the interface between the infused oil and the working fluid. The SLIPS was first introduced by Wong *et al.* (2011) and its design aimed at having a self-repairing surface with pressure-stable omniphobicity. The two liquids, one infused and one working fluid, are chosen to be immiscible and maintain a flat interface. The interface between the working fluid and lubricant is much more stable than that of the SHS, as the lubricant inside micro-grooved structures can withstand higher pressure fluctuations and physical stresses. Although the viscosity ratio of water to oil is much lower than that of the SHS and thus a lower drag reduction is expected for LIS than for SHS, a larger groove pitch length of LIS can be implemented owing to its pressure-stable characteristics, and possibly results in drag reduction comparable to that of SHS.

Although there have been several experimental studies on laminar flow over LIS including the drainage of the infused liquid and the interface instability (see, for example, Wexler, Jacobi & Stone (2015) and Liu *et al.* (2016)), there are limited experimental studies on drag reduction with LIS in laminar flows. Solomon, Khalil & Varanasi (2014) experimentally reported a drag reduction of 16 % with LIS for laminar flow in a cone and plate rheometer. In the case of turbulent flow, there are also only a few experimental studies dealing with LIS. Rosenberg *et al.* (2016) and Van Buren & Smits (2017) conducted experiments of Taylor–Couette flow with LISs. Rosenberg *et al.* (2016) reported that the amount of drag reduction remained relatively constant over the Reynolds number range tested and the LIS with heptane infused in the grooves produced up to 14 % drag reduction. Van Buren & Smits (2017) conducted similar experiments using square micro-grooves ($100 \sim 800$ μm) for various Reynolds numbers and achieved drag reduction exceeding 35 % with the groove width of $L_g^+ = L_g u_\tau / \nu_w \approx 35$, where u_τ is the wall shear velocity, and ν_w is the kinematic viscosity of water. Numerical studies considering the viscosity difference between the trapped and working fluids were conducted for idealized surfaces without supporting structures (Busse *et al.* 2013) or with longitudinal or transverse grooves (Schönecker & Hardt 2013, 2015; Nizkaya, Asmolov & Vinogradova 2014; Schönecker *et al.* 2014; Li *et al.* 2017; Sun & Ng 2017; Ge *et al.* 2018), but these studies were limited to laminar flows. Fu *et al.* (2017) performed direct numerical simulations (DNS) of turbulent channel flow over LIS with longitudinal and transverse grooves and confirmed the drag reducing capability of LIS. They investigated the effect of different viscosity ratios between the working and infused fluids, and conducted simulations where the grooves were overfilled with the lubricant so that a thin film of the lubricant was present over no-slip ridges. They suggested an effective slip-length model for the overfilled surfaces by combining the Stokes flow model of Schönecker *et al.* (2014) with the gas cushion model of Vinogradova (1995). The results were compared with their DNS data. However, the slip characteristics at the lubricated surfaces have not been investigated in detail. More recently, Cartagena *et al.* (2018) performed DNS of flow over an LIS with staggered cubic posts, where the interface was tracked with a level-set method. When the lubricant fraction was very large (e.g. 0.875), the drag was largely affected by the interface dynamics and even increased. However, for dense surface (e.g. lubricant fraction of 0.5), the interface deformation was relatively small and insensitive to the Weber number, and thus the instability of the interface was small for aligned micro-posts and longitudinal micro-grooves. Both studies on turbulent flow were carried out with somewhat fictitious material properties (e.g. the density ratio of the working fluid to the infused was kept as one).

We perform direct numerical simulations of a turbulent channel flow in order to investigate the slip characteristics of LIS (oil–water) with realistic material properties. The working fluid is water and the one infused is an oil such as FC-70, FC-3283 and heptane. For the supporting structure, we consider longitudinal grooves. This is because, according to Cheng, Teo & Khoo (2009), the longitudinal grooves performed best among four different SHS structures of square posts, square holes, transverse and longitudinal grooves in laminar channel flow. We also simulate turbulent channel flow with SHS (air–water) having the same structure geometry for comparison. The interfaces are assumed to be flat, and the surface-tension effect is neglected (Jung *et al.* 2016; Fu *et al.* 2017), which holds as the Weber number (or the capillary number) is very small for micro-size configurations. At a small Weber number, the capillary force is dominant over the inertial force of the flow, so the flow is prevented from

invading into the grooves and the lubricant can be kept inside the grooves whether it is oil (Fu *et al.* 2017; Van Buren & Smits 2017) or air (Cottin-Bizonne *et al.* 2004; Ybert *et al.* 2007; Teo & Khoo 2009). The shear-free boundary condition, mostly used for SHS, may be acceptable for SHS due to the high viscosity ratio of water to air ($\mu_{water}/\mu_{air} \simeq 55.56$). However, as the viscosity ratio of water to lubricating oil is not so high for LIS, we solve both the water and lubricant flows. The flow rate of water inside the channel is maintained constant, and a lubricant layer under the interface is shear driven by the turbulent water flow above. Numerical details are given in § 2. The drag reduction capabilities by LIS and SHS and the slip characteristics are discussed in § 3. In § 4, we obtain the effective slip lengths from the DNS data and suggest a predictive model as a function of the geometric parameters and lubricant viscosity. The effective slip lengths are then used to predict the drag reduction with LIS and SHS. A summary and conclusions are given in § 5.

2. Numerical details

2.1. *Governing equations and numerical method*

The governing equations are the incompressible Navier–Stokes and continuity equations,

$$\rho_\varphi \left(\frac{\partial u_i}{\partial t} + \frac{\partial}{\partial x_j} u_i u_j \right) = \Pi_\varphi \delta_{1i} - \frac{\partial p}{\partial x_i} + \mu_\varphi \frac{\partial^2 u_i}{\partial x_j \partial x_j} + f_i, \tag{2.1}$$

$$\frac{\partial u_i}{\partial x_i} - q = 0, \tag{2.2}$$

where x_i are the Cartesian coordinates (x, y, z), u_i are the corresponding velocity components (u, v, w), p is the pressure, ρ and μ are the density and viscosity of the fluid, respectively, the subscript φ indicates water or oil (or air), Π is the mean pressure gradient imposed on the water flow to maintain a constant mass flow rate ($\Pi = 0$ in the shear-driven oil or air layer). The values of f_i and q are the momentum forcing and mass source to satisfy the no-slip boundary condition and mass conservation on the longitudinal groove surfaces using an immersed boundary method (Kim, Kim & Choi 2001). Details of the determination of f_i and q are given in Kim *et al.* (2001).

To solve (2.1) and (2.2), a semi-implicit fractional-step method, adopting a third-order Runge–Kutta method for convection terms and the Crank–Nicolson method for viscous terms, is used for time integration,

$$\begin{aligned} \frac{\hat{u}_i^k - u_i^{k-1}}{\Delta t} = {} & \frac{2\alpha_k}{\rho_\varphi} \left(\Pi_\varphi^{k-1} \delta_{1i} - \frac{\partial p^{k-1}}{\partial x_i} \right) + \alpha_k [L_i(\hat{\boldsymbol{u}}^k) + L_i(\boldsymbol{u}^{k-1})] \\ & - \beta_k N_i(\boldsymbol{u}^{k-1}) - \gamma_k N_i(\boldsymbol{u}^{k-2}) + \frac{1}{\rho_\varphi} f_i^k, \end{aligned} \tag{2.3}$$

$$\frac{\partial^2 \phi^k}{\partial x_i \partial x_i} = \frac{1}{2\alpha_k \Delta t} \left(\frac{\partial \hat{u}_i^k}{\partial x_i} - q^k \right), \tag{2.4}$$

$$u_i^k = \hat{u}_i^k + 2\alpha_k \Delta t \left[(\Pi_\varphi^k - \Pi_\varphi^{k-1}) \delta_{1i} - \frac{\partial \phi^k}{\partial x_i} \right], \tag{2.5}$$

$$p^k = p^{k-1} + \rho_\varphi \phi^k - \mu_\varphi \alpha_k \Delta t \frac{\partial^2 \phi^k}{\partial x_j \partial x_j}, \tag{2.6}$$

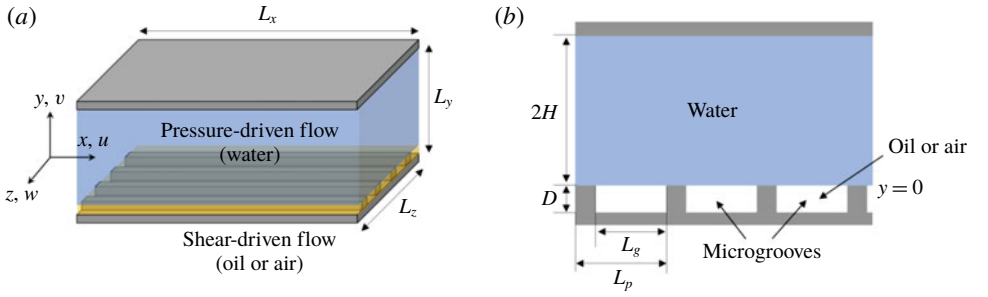

FIGURE 1. (Colour online) Schematic diagrams of the computational domain: (*a*) turbulent channel flow with micro-grooved structures; (*b*) cross-flow plane. Micro-grooved structures are placed only on the lower wall. Here, H is the channel half-height, D and L_g are the depth and width of micro-grooves, respectively, and L_p is the pitch length.

$$L_i(\boldsymbol{u}) = \nu_\varphi \frac{\partial^2 u_i}{\partial x_j \partial x_j}, \quad N_i(\boldsymbol{u}) = \frac{\partial}{\partial x_j} u_i u_j, \tag{2.7a,b}$$

where $\hat{u}_i$ are the intermediate velocity components, ϕ is the pseudo-pressure, ν_φ is the kinematic viscosity of water or oil (or air), the subscript $k(=1, 2, 3)$ is the sub-step index during one time step, Δt is the size of the computational time step and $\alpha_1 = 4/15$, $\alpha_2 = 1/15$, $\alpha_3 = 1/6$, $\beta_1 = 8/15$, $\beta_2 = 5/12$, $\beta_3 = 3/4$, $\gamma_1 = 0$, $\gamma_2 = -17/60$ and $\gamma_3 = -5/12$. Details of how to obtain Π_φ^k in (2.5) are described in You, Choi & Yoo (2000). The present numerical simulation is based on a finite volume method on a staggered grid system, and thus the velocity components are located at the cell faces, and the pressure is located at the cell centre. All spatial derivatives are discretized with the second-order central difference scheme. The maximum Courant–Friedrichs–Lewy (CFL) number varies from 0.7 to 1.4, depending on the oil used. Air-lubricated cases require smaller maximum CFL numbers than oil-lubricated ones, due to large differences in material properties across the interface.

Figure 1 shows the computational domain and the coordinate system used in the present study. The upper wall is a flat plate, but the lower wall has micro-size longitudinal grooves. The size of longitudinal grooves is determined with reference to the experiments of Woolford *et al.* (2009) and Rosenberg *et al.* (2016) in which the pitch length L_p is of the order of one in wall units. We summarize the cases of micro-grooves considered and numbers of grid points used for simulations in table 1, where $L_{p_o}^+ = L_p u_{\tau_o}/\nu_w$, $L_{g_o}^+ = L_g u_{\tau_o}/\nu_w$, $D_o^+ = D u_{\tau_o}/\nu_w$ and $u_{\tau_o}(=\sqrt{\tau_{w_o}/\rho_w})$ and τ_{w_o} are the wall-shear velocity and stress in the absence of micro-grooved structures, respectively. Here, the lubricant fraction is fixed at $\Phi = L_g/L_p = 0.8$; it is known that more drag reduction is achieved with larger Φ (Park *et al.* 2013, 2014), but the interface becomes less stable at the same time (Cartagena *et al.* 2018), and $\Phi = 0.8$ is the one used in Woolford *et al.* (2009). The size of the computational domain is $L_x = 3H$, $L_y = 2H + D$, $L_z = 0.84H$, where H is the channel half-height. The spanwise domain size is set to be slightly bigger than that of the minimal channel (Jiménez & Moin 1991) because low-order turbulence statistics near the wall are well predicted with minimal channel unit, and a large number of grid points is required in the z-direction due to micro-size grooves (see table 1). The periodic boundary condition is imposed in the x and z-directions. No-slip boundary condition is imposed on the upper wall and is satisfied on the longitudinal groove surfaces using an immersed boundary method (Kim *et al.* 2001).

Groove pitch		Groove width		Number of micro-grooves in L_z	Groove depth		Number of grid points (N_x, N_y, N_z)
L_p/H	L_{po}^+	L_g/H	L_{go}^+		D/H	D_o^+	
0.021	3.78	0.0168	3	40	0.02	3.6	(33, 129 + 32, 1200)
					0.04	7.2	(33, 129 + 32, 1200)
					0.08	14.4	(33, 129 + 64, 1200)
0.042	7.56	0.0336	6	20	0.02	3.6	(33, 129 + 32, 1200)
					0.04	7.2	(33, 129 + 32, 1200)
					0.08	14.4	(33, 129 + 64, 1200)
0.084	15.12	0.0668	12	10	0.02	3.6	(33, 129 + 32, 1200)
					0.04	7.2	(33, 129 + 32, 1200)
					0.08	14.4	(33, 129 + 64, 1200)

TABLE 1. Geometric parameters of grooves and number of grid points used.

We assume that the oil–water and air–water interfaces are flat (Jung *et al.* 2016). As discussed in § 1, this assumption is valid for the present study because the groove geometry under consideration is micro-sized and the corresponding Weber number using wall variables is of the order of 10^{-3}, $We^+ = \rho_w u_\tau^2 \delta_v/\sigma = \rho_w u_\tau \nu_w/\sigma = O(10^{-3})$ (Seo *et al.* 2015, 2018, see below), where u_τ is the friction velocity with the interface, δ_v is the viscous unit length ($\delta_v = \nu_w/u_\tau$) and σ is the surface-tension coefficient of water. The wall-parallel velocity components and shear stresses are continuous across the interface: i.e.

$$u_{w,s} = u_{l,s} = u_s, \quad w_{w,s} = w_{l,s} = w_s, \tag{2.8a,b}$$

$$\mu_w \left.\frac{\partial u_w}{\partial y}\right|_s = \mu_l \left.\frac{\partial u_l}{\partial y}\right|_s, \quad \mu_w \left.\frac{\partial w_w}{\partial y}\right|_s = \mu_l \left.\frac{\partial w_l}{\partial y}\right|_s. \tag{2.9a,b}$$

Here, the subscripts w, l and s stand for water, lubricant (oil or air) and the interface, respectively. The wall-normal velocity at the interface is zero, satisfying the impermeability condition

$$v_{w,s} = v_{l,s} = v_s = 0. \tag{2.10}$$

The slip velocity at the interface, (u_s, w_s), is obtained by taking one-side finite difference on (2.9) for each fluid, i.e.

$$\mu_w \frac{u_{upper} - u_s}{y_{upper} - y_s} = \mu_l \frac{u_s - u_{lower}}{y_s - y_{lower}}, \quad \mu_w \frac{w_{upper} - w_s}{y_{upper} - y_s} = \mu_l \frac{w_s - w_{lower}}{y_s - y_{lower}}, \tag{2.11a,b}$$

where $y_s(=0)$ is the y location of the interface, and y_{upper} and y_{lower} are the cell centre locations right above and below y_s, respectively, and u_{upper} and w_{upper}, and u_{lower} and w_{lower} are the corresponding slip velocity components. The boundary condition of the pseudo-pressure at the interface (for solving (2.4)) is given as

$$\left.\frac{\partial \phi_w}{\partial y}\right|_s = \left.\frac{\partial \phi_l}{\partial y}\right|_s = 0. \tag{2.12}$$

Equation (2.3) is solved using an alternating directional implicit scheme with the interface boundary conditions (2.8)–(2.10). The Poisson equation (2.4) is Fourier transformed in the x- and z-directions due to the periodic boundary conditions applied (this is possible even inside the groove because we use an immersed boundary

Lubricants	μ_l/μ_w	ρ_l/ρ_w	DR (%)
FC-70 (LIS)	23	1.94	−0.6
FC-3283 (LIS)	1.5	1.83	1.6
Water (rough)	1	1	0.7
Water (interface)	1	1	1.3
Heptane (LIS)	0.37	0.684	4.4
Air (SHS)	0.018	0.0012	5.1

TABLE 2. Lubricants and their viscosities and densities normalized by those of water, and the percentages of drag reduction (DR) for the case of $L_{g_o}^+ = 3$ ($L_{p_o}^+ = 3.78$) and $D_o^+ = 3.6$.

method), and the resulting tridiagonal system of equations is separately solved for two domains (below and above the interface, respectively) with the boundary condition (2.12).

The bulk Reynolds number is $Re = 2\rho_w u_b H/\mu_w = 5600$ corresponding to $Re_{\tau_o} = \rho_w u_{\tau_o} H/\mu_w \approx 180$, where u_b is the bulk velocity. The mass flow rate of water is maintained to be constant by imposing the mean pressure gradient Π, where Π is determined by obtaining the mean and fluctuating pseudo-pressure gradients separately at each time step (You *et al.* 2000).

2.2. *Lubricants and air*

For LIS, various oils can be utilized as long as they are immiscible with the working fluid (water) and maintain a flat interface. Considered lubricants are listed in table 2, together with their viscosities and densities. FC-70 is an oil used in Wong *et al.* (2011) with which the SLIPS was first introduced, whereas FC-3283 and heptane are oils used in Rosenberg *et al.* (2016), which reported drag reductions with LISs for turbulent Taylor–Couette flow. The Weber numbers for SHS and LIS (heptane) are $We^+ = \rho_w u_{\tau_o} v_w/\sigma = 1.29 \times 10^{-3}$ and 1.89×10^{-3}, respectively, for the case of $Re_{\tau_o} \approx 180$ and $L_{p_o}^+ = 3.78$ ($L_p = 0.021H$; $L_p = 40$ μm) (Woolford *et al.* 2009). Another Weber number suggested by Seo *et al.* (2018) is $We_L = \rho_w u_{\tau_o}^2 L_p/\sigma = We^+ L_p^+$. With $L_{p_o}^+ = 3.78$–15.12, $We_L = (4.91$–$19.66) \times 10^{-3}$ for SHS and $(7.14$–$28.58) \times 10^{-3}$ for LIS (heptane), respectively. Since these Weber numbers are small, the interface can be assumed to be flat.

The amounts of drag reduction (DR whose definition is given in § 3) with LISs from preliminary DNSs are shown in table 2 for the case of $L_{g_o}^+ = 3$ ($L_{p_o}^+ = 3.78$) and $D_o^+ = 3.6$ ($D = 0.02H$). In table 2, we add two more cases of 'water lubricant'. The case of water (rough) is to purely represent the effect of the groove geometry just like flow over riblets (Walsh 1983; Choi, Moin & Kim 1993; Bechert *et al.* 1997): i.e. the grooves are wet by the overlying water flow and act like a rough surface. The computational domain size in the y-direction is modified such that the bottom of micro-groove structures is at $y = -0.004H$, then the whole cross-sectional area of water flow in the presence of micro-groove structures is the same as that of flat-plate channel flow ($2H \times L_z$). The case of water (interface) is to replace oil with water but maintaining the flat interface: i.e. the lubricating water layer is shear driven, whereas the working fluid (water) is pressure driven, as in figure 1. These two cases of water (rough) and water (interface) do not show significant changes in the drag due to the small size of the grooves. On the other hand, the case of heptane shows a meaningful amount of drag reduction, comparable to that of SHS. The amounts of drag variation by FC-70 and FC-3283 are much smaller than that by heptane. Therefore, we choose heptane (LIS) and air (SHS) as the lubricating materials hereinafter.

	Domain size (L_x, L_y, L_z)	Number of grid points (N_x, N_y, N_z)	Grid resolution (Δx^+, Δz^+)	DR (%)	Mean slip velocity ($\bar{u}_s^{tot}/u_b$)
LIS	$(3H,\ 2H+D,\ 0.84H)$	(32, 193, 1200)	(16.7, 0.12)	12.7	0.165
	$(3H,\ 2H+D,\ 0.84H)$	(64, 193, 1200)	(8.4, 0.12)	11.0	0.160
	$(3H,\ 2H+D,\ 0.84H)$	(32, 193, 2400)	(16.7, 0.06)	12.6	0.169
	$(6H,\ 2H+D,\ 3.024H)$	(64, 193, 4320)	(16.7, 0.12)	13.9	0.162
SHS	$(3H,\ 2H+D,\ 0.84H)$	(32, 193, 1200)	(16.7, 0.12)	21.1	0.251
	$(3H,\ 2H+D,\ 0.84H)$	(64, 193, 1200)	(8.4, 0.12)	21.0	0.248
	$(3H,\ 2H+D,\ 0.84H)$	(32, 193, 2400)	(16.7, 0.06)	21.8	0.257
	$(6H,\ 2H+D,\ 3.024H)$	(64, 193, 4320)	(16.7, 0.12)	23.7	0.248

TABLE 3. Effects of the computational domain size and grid resolution on the drag reduction (DR; equation (3.2)) and mean slip velocity ($\bar{u}_s^{tot}$; see below for the definition) for LIS (heptane) and SHS (air) of $L_{g_o}^+ = 12$ and $D_o^+ = 14.4$.

2.3. *Effect of the computational domain size and grid resolutions*

As mentioned earlier, the present computational domain ($L_x = 3H$, $L_z = 0.84H$) is slightly bigger in the spanwise direction than that of the minimal channel (Jiménez & Moin 1991). Also, MacDonald *et al.* (2017) suggested a minimal computational domain size for a rough-wall turbulent flow such as $L_x^+ \geqslant 3L_z^+$ and $L_x^+ \geqslant 1000$. The first condition by MacDonald *et al.* (2017) is satisfied for the present domain size, but the second condition is not satisfied. Therefore, to confirm the appropriateness of the present computational domain size in the presence of lubricants, we conduct simulations in a larger computational domain ($L_x = 6H$ ($L_x^+ = 1080$) and $L_z = 3.024H$) for the case of $L_{g_o}^+ = 12$ ($L_{p_o}^+ = 15.12$) and $D_o^+ = 14.4$. Additional simulations with higher grid resolutions are also performed. The results are given in table 3. As shown, the changes in the amount of drag reduction and mean slip velocity due to the changes in the resolution and domain size are only approximately 3 %. Therefore, the present computational domain size and grid resolutions are appropriate to study the effects of LIS and SHS on near-wall turbulent flow.

3. Drag and slip characteristics

Given a fixed mass flow rate, the mean pressure gradient in the channel varies at each time step, balanced by the skin frictions on the upper flat surface and the lower longitudinal groove surface. Since the lubricant layer is shear driven by the water flow, the sum of skin frictions on the side and bottom surfaces of the groove structure is the same as the skin friction on the interface. Thus, the drags on the upper flat and lower groove surfaces are calculated as

$$\left.\begin{aligned} D_{upper\,wall} &= \frac{1}{T}\int_0^T\int_0^{L_x}\int_0^{L_z} \mu_w \frac{\partial u}{\partial y}(x,\, y=2H,\, z,\, t)\,\mathrm{d}z\,\mathrm{d}x\,\mathrm{d}t = L_x L_z \mu_w \left.\frac{\partial \bar{u}^{tot}}{\partial y}\right|_{upper\,wall}, \\ D_{groove} &= \frac{1}{T}\int_0^T\int_0^{L_x}\int_0^{L_z} \mu_w \frac{\partial u}{\partial y}(x,\, y=0,\, z,\, t)\,\mathrm{d}z\,\mathrm{d}x\,\mathrm{d}t = L_x L_z \mu_w \left.\frac{\partial \bar{u}^{tot}}{\partial y}\right|_{s}, \end{aligned}\right\} \tag{3.1}$$

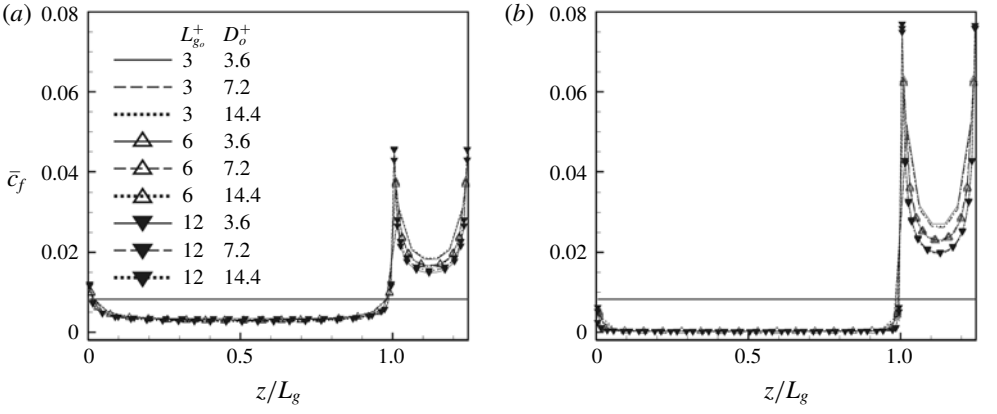

FIGURE 2. Spanwise variations of the friction coefficient ($\bar{c}_f$) on the interface and ridge: (*a*) heptane; (*b*) air. A horizontal line in (*a*,*b*) denotes the skin friction coefficient ($c_{f_o} = 0.0083$) of flat-plate turbulent channel flow at $Re_{\tau_o} = 180$.

respectively. Here, the superscript '*tot*' denotes the averaging over time and space (x and z). The drag reduction is calculated as

$$DR(\%) = \frac{D_{upper\,wall} - D_{groove}}{D_{upper\,wall}} \times 100. \tag{3.2}$$

This definition relies on the observation that turbulent flow near one side of the channel does not affect the skin friction on the other side of the channel (Jiménez & Moin 1991); the correlation coefficients between the shear rates at the two walls are small, $|corr| \leqslant 0.2$, for all the cases considered. The wall-shear rates are integrated over more than $800H/u_b$, and the amounts of drag reduction are listed in table 4 for the heptane- and air-lubricated cases. The drag reduction increases with increasing groove width ($L_{g_o}^+$) for all the groove depths (D_o^+) considered. On the other hand, given $L_{g_o}^+$, the amount of drag reduction is more or less saturated even with increasing D_o^+ (non-monotonic behaviours of the drag reduction with the groove depth in table 4 should be regarded as a result of numerical uncertainty). Although the air layer produces larger drag reductions for the same groove sizes than the heptane layer, the amount of drag reduction by the heptane layer is still not small. Note also that a similar drag reduction is achieved when the groove width of the heptane layer is twice that of the air layer. Considering that the interface of the heptane layer is more stable under the turbulent pressure fluctuations than that of the air layer, the LIS can be an alternative to the SHS as a device for drag reduction.

The spanwise variations of the time- and streamwise-averaged friction coefficient on the interface and ridge, $\bar{c}_f(z)$, are shown in figures 2(*a*) and 2(*b*) for the cases of heptane and air, respectively, where $c_f = \tau_s/(0.5\rho_w u_b^2)$, τ_s is the instantaneous shear stress, and the overbar denotes the averaging over the streamwise direction and time. The friction coefficients are lower on the heptane–water and air–water interfaces than that of flat plate channel flow, but are much higher on the ridge, especially near the corners ($z/L_g = 1$ and 1.25). Since the viscosity of air ($\mu_R = \mu_w/\mu_a = 55.56$) is much smaller than that of heptane ($\mu_R = \mu_w/\mu_l = 2.7$), the friction coefficient on the air–water interface is smaller (almost zero except near the corners) than that on the heptane–water interface, but the one on the ridge is higher because of large

	Heptane (LIS)			Air (SHS)		
	$L_{g_o}^+$			$L_{g_o}^+$		
D_o^+	3	6	12	3	6	12
3.6	4.4 %	6.6 %	11.8 %	5.1 %	12.3 %	18.3 %
7.2	3.0 %	7.0 %	12.0 %	7.2 %	10.4 %	23.0 %
14.4	4.6 %	9.1 %	12.7 %	7.0 %	12.7 %	21.1 %

TABLE 4. Drag reductions for the cases of heptane (LIS) and air (SHS).

	Heptane (LIS)	Air (SHS)	Shear-free condition
$\bar{c}_{f\,ridge}$	0.0224	0.0334	0.0339
$\bar{c}_{f\,interface}$	0.0038	0.00049	0
$\bar{c}_f^{tot}$	0.00752	0.00707	0.00678

TABLE 5. Skin friction coefficients on the ridge and interface, and total skin friction coefficients for LIS and SHS ($L_{g_o}^+ = 6, D_o^+ = 7.2$, and $\Phi = 0.8$), and those with the shear-free condition ($L_{g_o}^+ = 6$, $\Phi = 0.8$), respectively. Here, $\bar{c}_{f\,ridge}$ and $\bar{c}_{f\,interface}$ denote the mean skin friction coefficients on the ridge and interface, and $\bar{c}_f^{tot} = (1-\Phi)\bar{c}_{f\,ridge} + \Phi\bar{c}_{f\,interface}$.

slip velocity on the air–water interface (see below). The friction coefficient on the interface is nearly insensitive to the size of the groove (both L_g and D). On the other hand, the friction on the ridge is insensitive to D but depends on L_g. With increasing L_g, it decreases at the centre region but increases near the corner. As shown in this figure, higher drag reduction by the air layer than by the heptane layer is attributed to nearly zero shear stress at the interface, showing the validity of applying the shear-free boundary condition at the interface without solving the air layer, as demonstrated by previous studies (Martell *et al.* 2009, 2010; Park *et al.* 2013; Jelly *et al.* 2014; Türk *et al.* 2014; Lee *et al.* 2015; Rastegari & Akhavan 2015; Seo *et al.* 2015; Seo & Mani 2016; Rastegari & Akhavan 2018). We perform an additional simulation with the shear-free boundary condition at the interface for the case of $L_{g_o}^+ = 6$ and $\Phi = 0.8$, and the results are given in table 5 together with those from LIS and SHS. When the shear-free boundary condition is applied at the interface, the predicted $\bar{c}_f^{tot}$ results in only 4 % error for SHS (air), but in much larger error (approximately 10 %) for LIS (heptane) due to non-negligible shear stress at the interface.

Figure 3 shows the spanwise variations of the time- and streamwise-averaged slip velocity on the heptane–water and air–water interfaces. Each slip velocity has a profile similar to $\bar{u}_s(z^*)/\bar{u}_s(z^* = 0.5) = 2\sqrt{z^*(1-z^*)}(z^* = z/L_g)$ and is maximum at the centre of the interface (this elliptic velocity profile is analytically obtained for laminar flow if the shear rate at the interface is assumed to be constant along the spanwise direction (Schönecker *et al.* 2014)). The slip velocity increases with L_g, reaching up to approximately $4u_{\tau_o}$ and $6u_{\tau_o}$ for the cases of heptane and air, respectively, but it is nearly insensitive to D (except for the heptane with $L_{g_o}^+ = 12$ and $D_o^+ = 3.6$). The variation of the mean friction coefficient, $\bar{c}_f^{tot}$, which is the average of $\bar{c}_f$ (figure 2) over the whole spanwise direction, with the slip velocity averaged over the interface and ridge, $\bar{u}_s^{tot} = \int_0^{L_p} \bar{u}_s(z)\,\mathrm{d}z/L_p$, is shown in figure 4. The $\bar{c}_f^{tot}$ almost linearly decreases with $\bar{u}_s^{tot}$. This trend is consistent with the linear

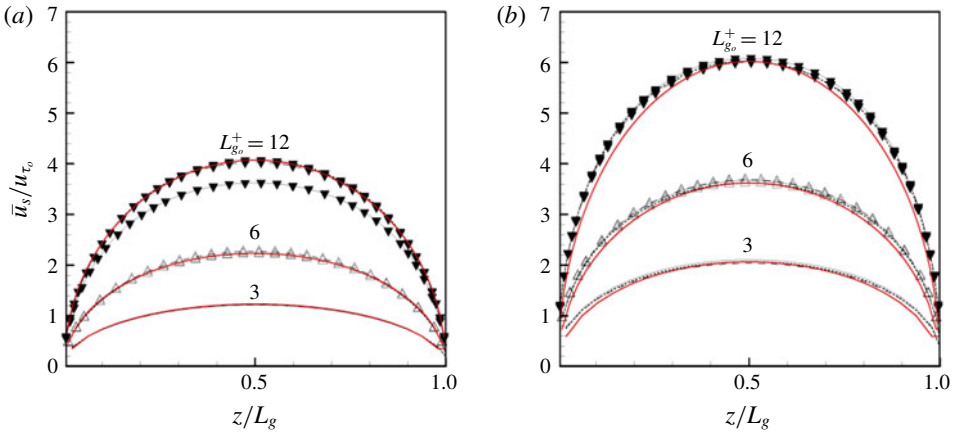

FIGURE 3. (Colour online) Slip velocity on the interface: (*a*) heptane; (*b*) air. Lines and lines with symbols are the same as those in figure 2. Red lines are the ellipses of $\bar{u}_s(z^*)/\bar{u}_s(z^* = 0.5) = 2\sqrt{z^*(1 - z^*)}$, where $z^* = z/L_g$.

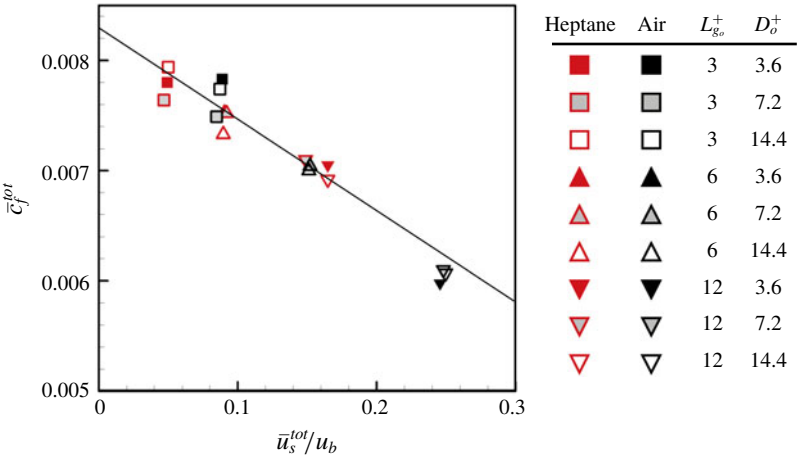

FIGURE 4. (Colour online) Mean friction coefficient versus mean slip velocity averaged over the interface and ridge. Solid line corresponds to the linear relation $\bar{c}_f^{tot}/c_{f_o} = 1 - (\bar{u}_s^{tot}/u_b)$ from Rastegari & Akhavan (2015). The friction coefficient of flat-plate turbulent channel flow is $c_{f_o} = 0.0083$ at $Re_{\tau_o} = 180$.

relation, $\bar{c}_f^{tot}/c_{f_o} = 1 - (\bar{u}_s^{tot}/u_b)$, suggested by Rastegari & Akhavan (2015), where c_{f_o} is the friction coefficient of flat-plate turbulent channel flow. Figure 5 shows the root-mean-square (r.m.s.) streamwise and spanwise slip velocity fluctuations at the interface. With increasing L_g, both $u_{s,rms}$ and $w_{s,rms}$ increase, and reach up to approximately u_{τ_o} and $0.2u_{\tau_o}$ for heptane, and $1.45u_{\tau_o}$ and $0.3u_{\tau_o}$ for air, respectively. Although the r.m.s. slip velocity fluctuations show some collapse for the same $L_{g_o}^+$, more deviations occur at larger $L_{g_o}^+$. Note also that the profiles of $u_{s,rms}$ and $w_{s,rms}$ follow the ellipses for smaller $L_{g_o}^+$.

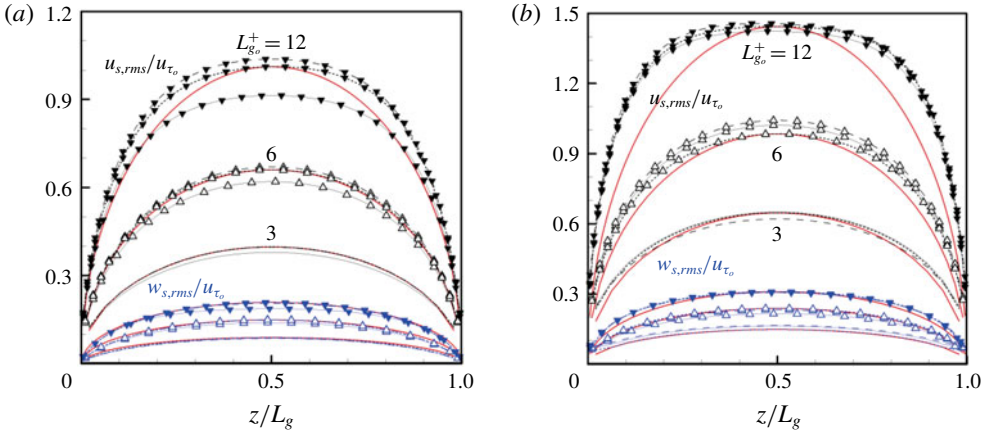

FIGURE 5. (Colour online) Root-mean-square (r.m.s.) slip velocity fluctuations normalized by the friction velocity u_{τ_o}: (*a*) heptane; (*b*) air. Lines and lines with symbols are the same as in figure 2. Red lines are the ellipses of $u_{is,rms}(z^*)/u_{is,rms}(z^* = 0.5) = 2\sqrt{z^*(1-z^*)}$ ($z^* = z/L_g$).

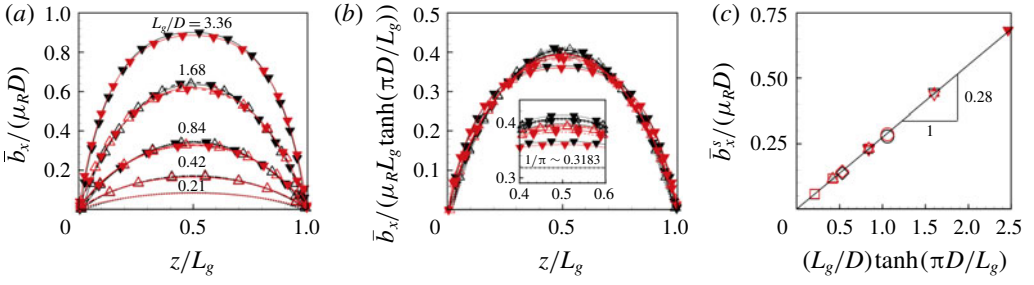

FIGURE 6. (Colour online) Normalized slip lengths: (*a*) slip length normalized by the groove depth and viscosity ratio; (*b*) slip length normalized as in (3.6) versus z/L_g; (*c*) mean slip length (3.6). In (*a*,*b*), the lines and lines with symbols are the same as in figure 2, where red and black colours denote the cases of heptane and air, respectively. In (*c*), the symbols are the same as those in figure 4, together with the cases of $L_{g_o}^+ = 3.8$ ($\Phi = 0.5$) and $D_o^+ = 3.6$ (○, red and ○, black), and $L_{g_o}^+ = 1.9$ ($\Phi = 0.5$) and $D_o^+ = 3.6$ (◇, red and ◇, black). Inset in (*b*) shows the slip length near the groove centre.

Since the slip velocity and velocity gradient vary over the interface, the slip length is also a function of the interface location as follows:

$$\bar{b}_x(z) = \frac{\bar{u}_s(z)}{\partial \bar{u}(z)/\partial y|_s}. \tag{3.3}$$

Figure 6 shows the slip lengths in different normalizations over the interface and the mean slip length for the cases of heptane and air. The slip length normalized by the groove depth and viscosity ratio $\mu_R (= \mu_w/\mu_l)$ is only a function of L_g/D irrespective of the lubricants, and they increase with increasing L_g/D (figure 6*a*). According to Jung *et al.* (2016) who considered the air–water interface in the absence of the ridges (i.e. an idealized SHS) for turbulent channel flow, the mean slip length divided by the

air layer thickness (D) is equal to the viscosity ratio μ_R, i.e.

$$\bar{b}_x^* = \frac{\bar{b}_x}{\mu_R D} = 1 \quad \text{(for an idealized SHS)}, \tag{3.4}$$

because of the linear velocity profile within the air layer. In the present micro-groove configuration, however, the flow is affected by the no-slip condition on the ridge of the groove structure, and thus the resulting slip length is less than one, i.e. $\bar{b}_x < \mu_R D$ (figure 6*a*), and is a function of L_g/D. When the groove is sufficiently wide as compared to its depth ($L_g/D \gg 1$), the normalized slip length should approach one (for $L_g/D = 3.36$, $\bar{b}_x/\mu_R D \approx 0.9$ at the groove centre).

Considering the shear-driven Stokes flow inside the longitudinal groove, Maynes *et al.* (2007) provided the velocity distribution inside the groove and the velocity gradient at the interface using the sine series expansion. Since the component corresponding to the largest wavelength is dominant, the slip length averaged over the interface can be approximated as (using the continuity of the shear stress at the interface)

$$\bar{b}_x^s = \frac{\displaystyle\int_0^{L_g} \bar{u}_s \,\mathrm{d}z}{\displaystyle\int_0^{L_g} \partial\bar{u}/\partial y|_s \,\mathrm{d}z} = \mu_R \frac{\displaystyle\int_0^{L_g} u_l|_s \,\mathrm{d}z}{\displaystyle\int_0^{L_g} \partial u_l/\partial y|_s \,\mathrm{d}z} \sim \frac{1}{\pi}\mu_R L_g \tanh\frac{\pi D}{L_g}. \tag{3.5}$$

Accordingly, the non-dimensional slip length from the Stokes flow approximation becomes

$$\bar{b}_x^{**} = \frac{\bar{b}_x^s}{\mu_R L_g \tanh(\pi D/L_g)} \sim \frac{1}{\pi}. \tag{3.6}$$

This result is very similar to that of Ybert *et al.* (2007), $\bar{b}_x = (1/q)\mu_R L_g \tanh(qD/L_g)$ (q is a function of Φ), which was obtained for a square array of dilute pillars based on the Stokes flow solution for the periodic arrays of spheres by Sangani & Acrivos (1982). Figure 6(*b*) shows the variations of the slip length, normalized as in (3.6), over the interface for all cases of heptane and air considered. The data scatter observed in figure 6(*a*) is much reduced by introducing a new normalization, (3.6). The normalized slip length at the groove centre region approaches $1/\pi$, as the groove becomes shallow for same L_g (i.e. increasing L_g/D). Figure 6(*c*) shows the mean slip lengths averaged over the interface as a function of L_g/D. As shown, all the data fall on a line whose slope is 0.28, i.e.

$$\bar{b}_x^s = 0.28\mu_R L_g \tanh\frac{\pi D}{L_g}. \tag{3.7}$$

Note that (3.7) returns to $\bar{b}_x^s/\mu_R D \sim 0.28\pi$ for $L_g \gg D$ and $\bar{b}_x^s/\mu_R L_g \sim 0.28$ for $L_g \ll D$. The proportional constant, theoretically obtained, in (3.5) is $1/\pi (= 0.3183)$, and thus the difference between (3.5) and (3.7) is only 12 %, indicating that the Stokes flow approximation inside the groove works quite well even for turbulent flows above the interface, as pointed out for small structures of $L_g^+ = L_g u_\tau/\nu_w < O(10)$ in Seo & Mani (2016). Since the cases discussed so far are for $\Phi = 0.8$, additional simulations are carried out for $\Phi = 0.5$ and two different geometries of $L_{g_o}^+ = 3.8$ and $D_o^+ = 3.6$, and $L_{g_o}^+ = 1.9$ and $D_o^+ = 3.6$. These cases also fall on the curve (3.7), as shown in figure 6(*c*). Table 6 shows the Reynolds numbers in the grooves, defined by the

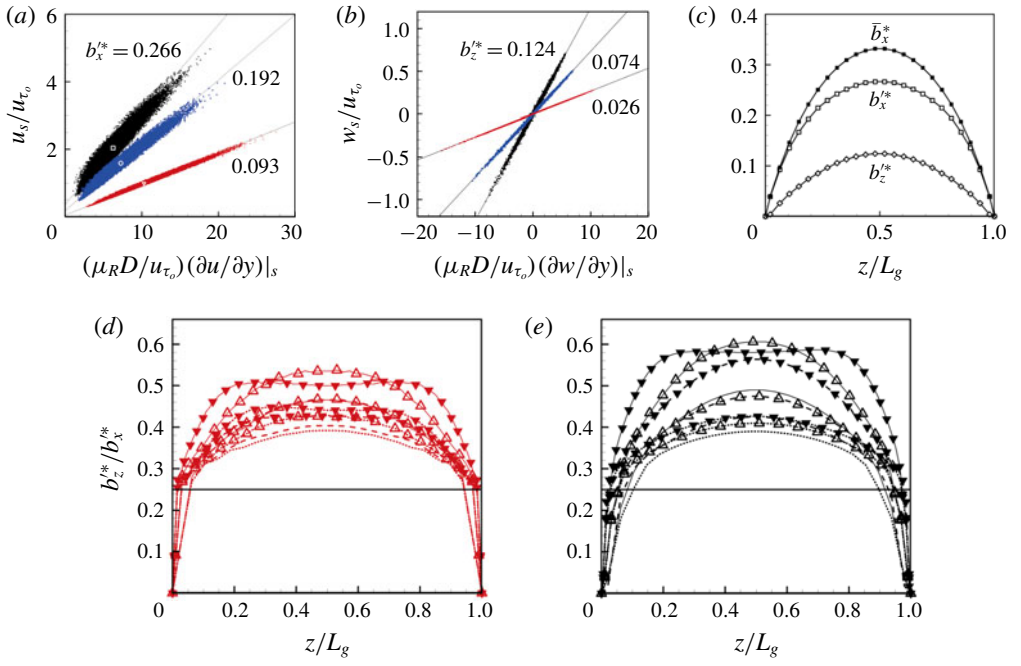

FIGURE 7. (Colour online) Scatter plots and slip lengths (heptane; $L_{g_o}^+ = 3$ and $D_o^+ = 3.6$): (*a*) u_s versus $\partial u/\partial y|_s$; (*b*) w_s versus $\partial w/\partial y|_s$; (*c*) mean streamwise slip length ($\bar{b}_x^*$), and fluctuating streamwise ($b_x'^*$) and spanwise ($b_z'^*$) slip lengths; (*d*,*e*) variations of $b_z'^*/b_x'^*$ over the interface for all the cases of heptane (*d*) and air (*e*), respectively. In (*a*,*b*), ▼, $z/L_g = 0.0625$; ●, 0.1875; ■, 0.479. The slopes of lines passing through $((\partial\bar{u}/\partial y|_s)/(u_{\tau_o}/\mu_R D), \bar{u}_s/u_{\tau_o})$ (denoted as white open symbols), obtained by a least-square method, in (*a*,*b*) correspond to $b_x'^*$ and $b_z'^*$, respectively. In (*d*,*e*), lines and lines with symbols are the same as in figure 2, and the horizontal line corresponds to $b_z'^*/b_x'^* = 1/4$ for an idealized SHS (Jung *et al.* 2016).

	Heptane (LIS)			Air (SHS)		
	$L_{g_o}^+$			$L_{g_o}^+$		
D_o^+	3	6	12	3	6	12
3.6	2.55	5.03	10.17	0.176	0.315	0.657
7.2	2.55	4.99	9.70	0.157	0.340	0.539
14.4	2.57	4.93	9.53	0.188	0.333	0.584

TABLE 6. Reynolds numbers in the grooves, $Re_{\tau_l} = u_{\tau_l} L_g/\nu_l$, where u_{τ_l} is the shear velocity at the interface and ν_l is the kinematic viscosity of the lubricant.

shear velocity at the interface and groove width, for the cases considered in the present study. As shown, the Reynolds numbers in the grooves are indeed very small, supporting the use of Stokes flow approximation inside the grooves.

The anisotropy of local slip in the streamwise and spanwise directions on SHS has been studied by Nizkaya *et al.* (2014) and Schönecker *et al.* (2014) for laminar flow, and by Jung *et al.* (2016) for turbulent flow. Figures 7(*a*) and 7(*b*) show the

scatter plots of the instantaneous streamwise and spanwise slip velocities versus their corresponding velocity gradients at the interface, respectively, for three different spanwise locations, together with their mean values of the streamwise components ($L_{g_o}^+ = 3$ and $D_o^+ = 3.6$). Here, the fluctuating slip lengths, b_x' and b_z', are obtained from the slopes of the lines passing through $(\partial\bar{u}/\partial y|_s/(u_{\tau_o}/\mu_R D),\ \bar{u}_s/u_{\tau_o})$ using a least-square method for the scattered data. Owing to the shear-driven flow along the longitudinal groove, the scatter in the spanwise component is much narrower than that in the streamwise component. Figure 7(*c*) shows the spanwise variations of the mean and fluctuating slip lengths, and figures 7(*d*) and 7(*e*) show the ratio of the fluctuating spanwise slip length to the streamwise one for heptane- and air-lubricated surfaces, respectively. The mean streamwise slip length is larger than the fluctuating streamwise and spanwise slip lengths, and the fluctuating streamwise slip length is larger than the spanwise one, which is consistent with the results of Seo & Mani (2016) and Fairhall & García-Mayoral (2018) for small textures of isotropic posts. The ratios of b_z' to b_x' vary along the spanwise direction (figure 7*d*,*e*), largest at the centre of the groove and smallest at the corners for most cases. The exceptions to this trend are those of $L_{g_o}^+ = 12$ and $D_o^+ = 3.6$, where b_z'/b_x' is relatively constant at the groove centre region but maximum at off-centre locations. These fluctuating slip-length ratios are less than 1, indicating that the slip is anisotropic. These ratios are larger than that for an idealized SHS ($b_z'/b_x' \sim 1/4$) except very near the corner, but smaller than those (0.896 and 0.909) for isotropic micro-posts of Seo & Mani (2016) with $L_{g_o}^+ = 4$ and of Fairhall & García-Mayoral (2018) with $L_{g_o}^+ = 8$ (both cases have the lubricant fraction of 8/9). This difference is due to the limitation of spanwise motion in the present streamwise micro-grooved structures.

Figure 8(*a*,*b*) shows the fluctuating streamwise and spanwise slip lengths normalized by $\mu_R L_g \tanh(\pi D/L_g)$, $b_x'^{**}$ and $b_z'^{**}$, for all cases considered in the present study. The normalized fluctuating slip lengths do not collapse, unlike the mean slip length (figure 6*b*). However, as shown in figure 8(*c*), the fluctuating spanwise slip lengths averaged over the interface fall on a line whose slope is 0.0856, i.e.

$$\overline{b_z'}^s = 0.0856\mu_R L_g \tanh(\pi D/L_g). \tag{3.8}$$

Equation (3.8) indicates that $\overline{b_z'}^s/\mu_R D \sim 0.0856\pi$ for $L_g \gg D$ and $\overline{b_z'}^s/\mu_R L_g \sim 0.0856$ for $L_g \ll D$. Equations (3.7) and (3.8) are used in the next section to evaluate the drag reduction performances by LIS and SHS.

4. Effective slip length and drag reduction

The effective slip length is defined as

$$b_{x,eff} \equiv \frac{\bar{u}_s^{tot}}{\partial\bar{u}^{tot}/\partial y|_s}, \tag{4.1}$$

where $\bar{u}_s^{tot}$ and $\partial\bar{u}^{tot}/\partial y|_s$ are the velocity and velocity gradient averaged over the interface and ridge of the micro-groove and also in time, respectively. Their values in wall units ($b_{x,eff}^+ = b_{x,eff}u_\tau/\nu_w$) are given in table 7, where $u_\tau (= \sqrt{\nu_w \partial\bar{u}^{tot}/\partial y|_s})$ is the friction velocity. As expected, the effective slip length of SHS (air) is larger than that of LIS (heptane). It is nearly insensitive to the groove depth but significantly depends on the groove width within the parameter ranges considered. As the groove widths considered in the present study are relatively small ($L_{g_o}^+ < O(10)$), the effective

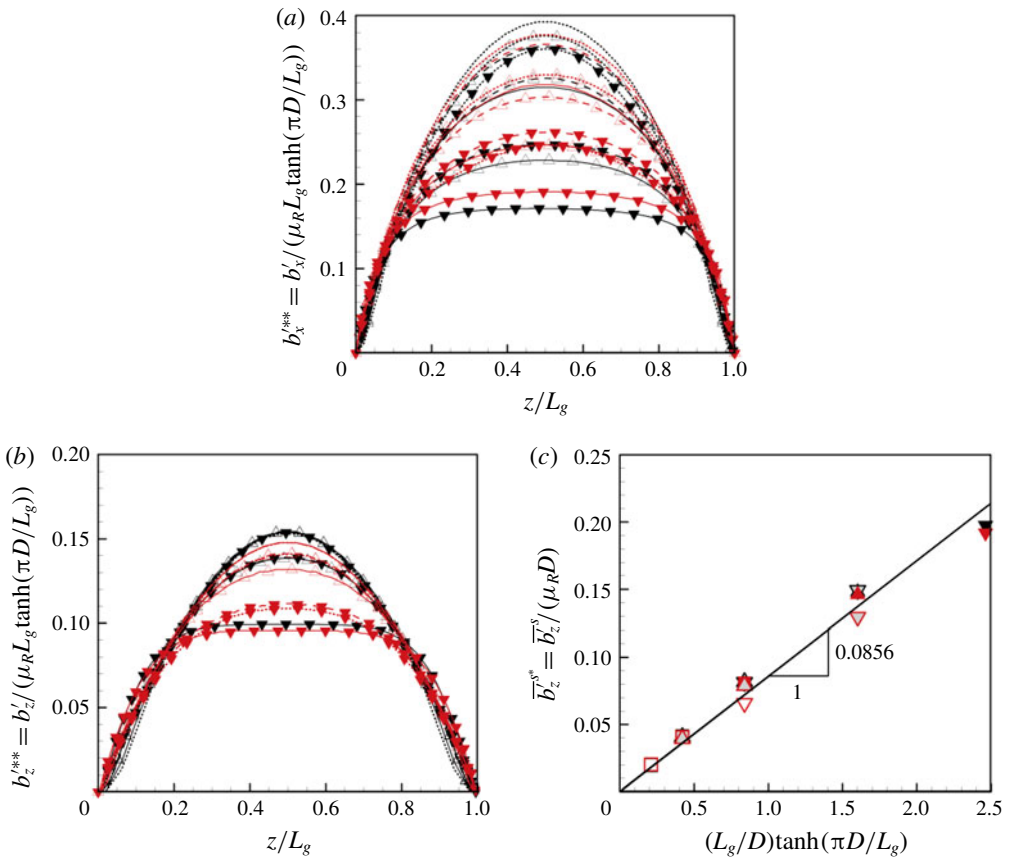

FIGURE 8. (Colour online) Non-dimensionalized fluctuating streamwise and spanwise slip lengths and averaged fluctuating spanwise slip length: (*a*) $b_x'^{**}$; (*b*) $b_z'^{**}$; (*c*) $\bar{b}_z'^{s^*}$. In (*a*,*b*), lines and lines with symbols are the same as in figure 2, and red and black colours denote the cases of heptane and air, respectively. In (*c*), symbols are the same as in figure 4.

	Heptane (LIS)			Air (SHS)		
	L_{go}^+			L_{go}^+		
D_o^+	3	6	12	3	6	12
3.6	0.79	1.47	2.49	1.41	2.56	4.53
7.2	0.79	1.50	2.76	1.39	2.58	4.54
14.4	0.79	1.49	2.80	1.44	2.55	4.55

TABLE 7. Effective slip lengths in wall units, $b_{x,eff}^+$, for the cases of heptane and air.

slip length shows a linear increase with increasing groove width. This is consistent with the result of Seo & Mani (2016) in which $b_{x,eff}^+ \sim L_g^+$ and $L_g^{+1/3}$ for SHSs with small and large texture sizes, respectively.

For a laminar flow, Belyaev & Vinogradova (2010) considered SHS with alternating slip (with constant slip length) and no-slip surfaces, and proposed theoretical relationships between the effective slip lengths ($b_{x_i,eff}$) and surface geometric parameters for longitudinal ($x_i = x$) and transverse ($x_i = z$) groove configurations as follows:

$$b_{x_i,eff} \simeq \frac{L_p \ln\left[\sec\left(\frac{\pi\Phi}{2}\right)\right]}{K_i + \frac{L_p}{\tilde{b}_{x_i}} \ln\left[\sec\left(\frac{\pi\Phi}{2}\right) + \tan\left(\frac{\pi\Phi}{2}\right)\right]}, \tag{4.2}$$

where $\tilde{b}_{x_i}$ are the constant slip lengths, and $K_i = \pi$ and 2π for the longitudinal and transverse grooves, respectively. Schönecker *et al.* (2014) obtained a slip-length distribution over the interface in the form of an ellipse (with maximum at the interface centre) by assuming a constant shear rate at the interface and proposed formulae for the effective slip lengths. The $\tilde{b}_x$ and $\tilde{b}_z$ in Schönecker *et al.* (2014), given as an error function, correspond to the maximum slip lengths at the centres of the longitudinal and transverse grooves, respectively. Schönecker *et al.* (2014) indicated that (4.2) with constant slip lengths $\tilde{b}_x$ and $\tilde{b}_z$, as done in Belyaev & Vinogradova (2010), underestimate the effective slip lengths. In figures 6(*c*) and 8(*c*), we already obtained the slip lengths averaged over the interface, $\bar{b}_x^s$ and $\bar{b}_z^{\prime s}$. Using this information, we can determine $\tilde{b}_x$ and $\tilde{b}_z$ in (4.2) by assuming the slip-length profile as an ellipse (from the ellipse profile of the slip velocity (figure 3) and nearly constant shear rate at the interface (figure 2); also assumed by Schönecker *et al.* (2014))

$$\left.\begin{aligned} \tilde{b}_x &= \frac{4}{\pi}\bar{b}_x^s = \frac{1.12}{\pi}\mu_R L_g \tanh(\pi D/L_g), \\ \tilde{b}_z &= \frac{4}{\pi}\bar{b}_z^{\prime s} = \frac{0.342}{\pi}\mu_R L_g \tanh(\pi D/L_g). \end{aligned}\right\} \tag{4.3}$$

The present model (4.3) is similar to that of Schönecker *et al.* (2014), in that the hyperbolic tangent function is close to the error function. Note that we use (4.2) for the present spanwise effective slip length because the flow inside the spanwise grooves can be approximated by Stokes flow under a constant shear, as in Schönecker *et al.* (2014).

The effective slip lengths are predicted using (4.2) and (4.3), and they are plotted against those from DNS in figure 9. Here, for DNS results, we obtain the streamwise effective slip length from (4.1) and the spanwise effective slip length from

$$b_{z,eff} = \frac{1}{2}\left(\frac{\bar{w}_s^{tot}|_{w_s \geqslant 0}}{\partial \bar{w}^{tot}/\partial y|_{s^{w_s} \geqslant 0}} + \frac{\bar{w}_s^{tot}|_{w_s < 0}}{\partial \bar{w}^{tot}/\partial y|_{s^{w_s} < 0}}\right), \tag{4.4}$$

because the spanwise velocity gradient averaged over the interface is zero for the present longitudinal micro-grooves. As shown in this figure, the predicted effective slip lengths from (4.2) and (4.3) are in excellent agreements with the DNS results, even for different Φ, although the effective spanwise slip lengths of SHS with $L_{g_o}^+ = 12$ show some disagreements.

Fukagata *et al.* (2006) suggested the following implicit relation between the effective slip length and drag reduction with SHS,

$$\frac{1}{\kappa}\ln Re_{\tau_o} + F_0 = \left(1 - \frac{DR}{100}\right) b_{x,eff_o}^+ + \frac{\sqrt{1 - DR/100}}{\kappa} \ln\left(\sqrt{1 - \frac{DR}{100}} Re_{\tau_o}\right)$$

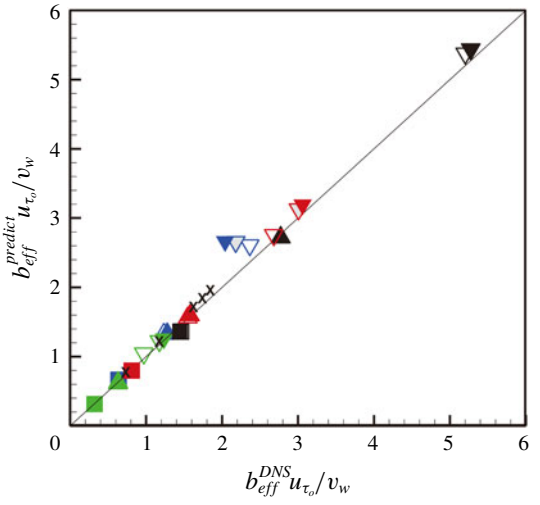

FIGURE 9. (Colour online) Predicted effective slip lengths in the streamwise and spanwise directions. ×, present model ((4.2) and (4.3)) with the DNS data of Fu *et al.* (2017; $\Phi = 0.5$); other symbols (same as in figure 4), from the present model with the present DNS data ($\Phi = 0.8$). The symbols outlined with red and black colours denote the streamwise effective slip length for heptane- and air-lubricated surfaces, while those outlined with blue and green colours denote the spanwise effective slip length for heptane and air- lubricated surfaces, respectively.

$$+\sqrt{1-\frac{DR}{100}}F\left(\sqrt{1-\frac{DR}{100}}b^+_{z,eff_o}\right), \tag{4.5}$$

$$F(\xi) = F_\infty + (F_0 - F_\infty)\exp[-(\xi/\alpha)^\beta], \tag{4.6}$$

where $b^+_{x,eff_o} = b_{x,eff}u_{\tau_o}/v_w$, $\kappa = 0.41$, $F_0 = 3.2$, $F_\infty = -0.8$, $\alpha = 7$ and $\beta = 0.7$ which were obtained from DNS data at $Re_b = 5600$ and 14 000. Busse & Sandham (2012) proposed a different F in (4.5)

$$F(\xi) = F_\infty + \frac{(F_0 - F_\infty)^2}{(F_0 - F_\infty) + \xi}, \tag{4.7}$$

where $F_0 = 3.0$ and $F_\infty = -1.0$, fitted for $Re_b = 5620$ and 12 500. Rastegari & Akhavan (2015) used the Fukagata–Iwamoto–Kasagi identity (known as the FIK identity, see Fukagata, Iwamoto & Kasagi (2002)) to derive an explicit relation between the effective slip length and drag reduction

$$DR(\%) = \frac{b^+_{x,eff_o}}{b^+_{x,eff_o} + \dfrac{Re_b}{Re_{\tau_o}}} \times 100. \tag{4.8}$$

On the other hand, from Rastegari & Akhavan (2018) and Fairhall & García-Mayoral (2018), the following relation (motivated by the drag reduction by riblets in terms of the protrusion heights; see Luchini, Manzo & Pozzi (1991), Jiménez (1994), Bechert *et al.* (1997), García-Mayoral & Jiménez (2011)) is introduced,

$$DR(\%) = 100(A\sqrt{1 + (A/2)^2} - A^2/2), \tag{4.9}$$

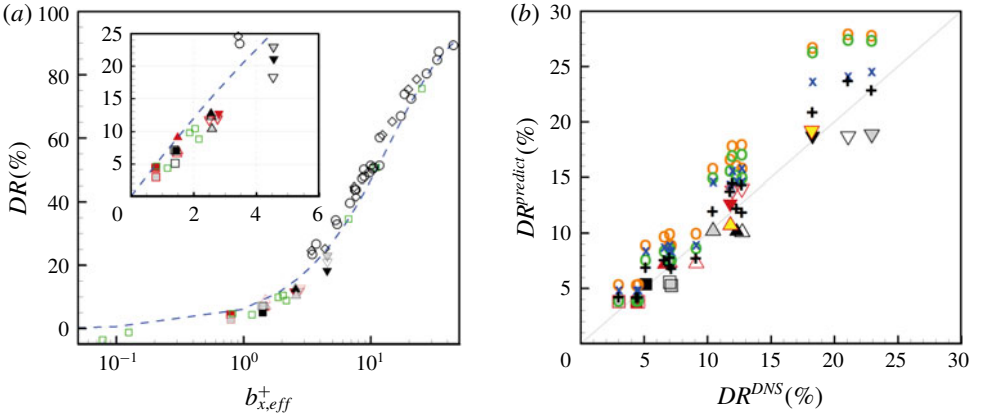

FIGURE 10. (Colour online) Drag reductions: (*a*) *DR* versus effective slip length in wall units ($b^+_{x,eff}$); (*b*) predicted drag reductions using various models. In (*a*), ○, Park *et al.* (2013); ◇, Jung *et al.* (2016); □ (green), Fu *et al.* (2017); - - -, (4.8) from Rastegari & Akhavan (2015); other symbols, present study (given in figure 4). In (*b*), ○ (green), (4.5) and (4.6) (Fukagata *et al.* 2006) with b^+_{x,eff_o} from present DNS; ○ (orange), (4.5) and (4.7) (Busse & Sandham 2012) with b^+_{x,eff_o} from present DNS; ×, (4.8) (Rastegari & Akhavan 2015) with b^+_{x,eff_o} from present DNS; +, (4.9) with Δh^+_o from present DNS; other symbols (same as in figure 4), (4.9) with modelled b^+_{x,eff_o} and b^+_{z,eff_o} from (4.2) and (4.3), where △ (yellow) and ▽ (yellow) and are predictions for $Re_{\tau_o} \approx 395$ (others are for $Re_{\tau_o} \approx 180$). Here, Re_{τ_o} in (4.5) and (4.8), and c_{f_o} in (4.9) are obtained from the upper flat surface.

where $A = (\mu_o \Delta h^+_o)/((2c_{f_o})^{-1/2} + (2\kappa)^{-1})$, $\Delta h^+_o = b^+_{x,eff_o} - b^+_{z,eff_o}$, $\kappa = 0.4$, $c_{f_o} \simeq 0.0083$ and $\mu_o = 0.785$. In the case of low drag reduction (i.e. $A \ll O(1)$), (4.9) can be written as (using the Taylor series expansion)

$$DR(\%) \approx 100(A^3/8 - A^2/2 + A). \tag{4.10}$$

The present drag reduction versus the effective slip length in wall units is shown in figure 10(*a*), together with those of Park *et al.* (2013), Jung *et al.* (2016), Fu *et al.* (2017) and (4.8). The present data collapse very well with the previous numerical data, but the present data and the data of Fu *et al.* (2017), having small effective slip lengths, are located slightly below (4.8).

Now, we predict the drag reductions from (4.5) and (4.6), (4.5) and (4.7), (4.8) and (4.9), respectively. The values of Re_{τ_o} and c_{f_o} are from the upper wall, and the effective slip lengths are either from DNS data or from (4.2) and (4.3), given the groove geometry (L_g, D, Φ) and material property (μ_R). Figure 10(*b*) shows the predicted drag reductions from various models. Overall, the prediction by (4.9) performs the best among these models. The predictions are good especially for small grooves because the Stokes flow assumption made for (4.2) and (4.3) is valid for those grooves (Seo & Mani 2016; Fairhall & García-Mayoral 2018). Equation (4.9) together with (4.2) and (4.3) is tested for a higher Reynolds number of $Re_{\tau_o} \approx 395$ with heptane-lubricated surfaces, where the groove geometries tested are $L_g/H = 0.0336$ and 0.0672, and $D/H = 0.04$, which correspond to $L^+_{g_o} = 13.3$ and 26.5, and $D^+_o = 15.8$. The computational domain size is $L_x = 3H$ and $L_z = 0.84H$, and the number of grid points used are $96(x) \times 193(y) \times 1200(z)$. As shown in figure 10(*b*) and table 8, the

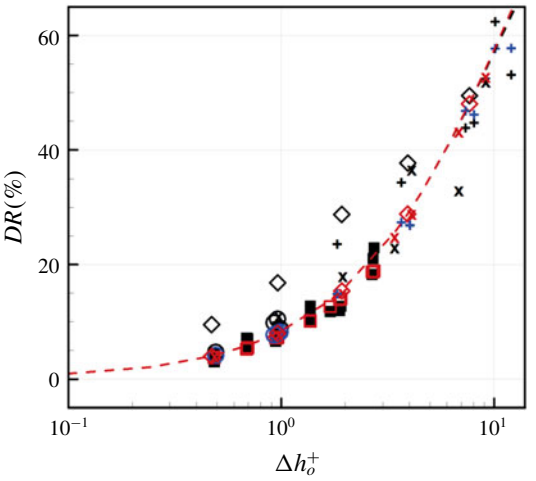

FIGURE 11. (Colour online) Drag reductions from DNS (SHS and LIS) and prediction by (4.9) with (4.2) and (4.3) with $\Delta h_o^+ (= b^+_{x,eff_o} - b^+_{z,eff_o})$: ■ and □, present study; ○ (black) and ○ (blue), Fu *et al.* (2017); + (black) and + (blue), Park *et al.* (2013); × (black) and × (red), Rastegari & Akhavan (2015, 2018); ◇ (black) and ◇ (red), Türk *et al.* (2014); - - - (black) and - - - (red), equations (4.9) and (4.10) with $c_{f_o} = 0.0083$, respectively. Here, the black- and red-coloured symbols are from DNS and predicted ones, respectively.

Groove size	b^{+DNS}_{x,eff_o}	$b^{+predict}_{x,eff_o}$	b^{+DNS}_{z,eff_o}	$b^{+predict}_{z,eff_o}$	DR^{DNS}	$DR^{predict}$
$L^+_{g_o} = 13.3$ and $D^+_o = 15.8$	3.44	3.65	1.37	1.43	11.8 %	10.7 %
$L^+_{g_o} = 26.5$ and $D^+_o = 15.8$	6.01	6.95	2.35	2.71	18.2 %	19.2 %

TABLE 8. Predicted effective slip lengths and drag reductions for $Re_{\tau_o} \approx 395$ (heptane).

predictions for the effective slip lengths and drag reduction are also excellent for a higher Reynolds number.

The DNS results from previous studies (Park *et al.* 2013; Türk *et al.* 2014; Rastegari & Akhavan 2015, 2018; Fu *et al.* 2017) are also used to validate the model, (4.9) with (4.2) and (4.3). Here, we select the cases of LIS and SHS with longitudinal grooves, and take $\tanh(\pi D/L_g) \approx 1$ for the data from the DNS with shear-free boundary condition at the interface. The comparison of these data with the predictive model is made in figure 11. As shown, the model agrees very well with the data from the present and other studies, except for those from Türk *et al.* (2014), indicating that (4.9) with (4.2) and (4.3) is a predictive model for drag reduction by SHS and LIS.

5. Conclusions

In the present study, we investigated the effects of heptane-lubricated micro-surfaces on the skin friction drag and slip characteristics in a turbulent channel flow at $Re_{\tau_o} \approx 180$ using direct numerical simulation. Nine different geometries of the longitudinal micro-groove structures (varying the width and depth of the rectangular groove cross-section) were examined: $L^+_{g_o} = 3$, 6 and 12, and $D^+_o = 3.6$, 7.2 and 14.4, respectively.

For all cases, the lubricant fraction was fixed at $\Phi = 0.8$. Same computations were also carried out for air-lubricated surfaces to understand the effects of the lubricating material viscosity. Considering the small Weber numbers involved, the interface was assumed to be flat, and both the turbulent water flows above the interface and flows inside the lubricant layer were simulated, from which the slip velocity and length were obtained at the interface.

The drag reduction increased with increasing groove width but was more or less saturated with the groove depth. The amount of drag reduction by the air-lubricated surface was larger than that of the heptane-lubricated surface because the air–water interface was almost shear free (as modelled as shear free in previous studies) but the shear rate on the heptane–water interface was not negligible. The mean streamwise slip velocity and the r.m.s. streamwise and spanwise slip velocity fluctuations varied with the groove width, but were relatively insensitive to the groove depth. The mean streamwise slip length and fluctuating spanwise slip length averaged over the interface were scaled well with the characteristic length, $\mu_R L_g \tanh(\pi D/L_g)$, obtained from the Stokes flow assumption in the lubricant layer.

It is known that the effective slip length in wall units is closely related to the drag reduction. Based on the present results, we proposed a model for the effective slip lengths in the streamwise and spanwise directions, and the predicted results agreed well with the present DNS data. Four different formulae for the prediction of drag reduction were examined together with the present effective slip length models. The predictions were in excellent agreements with those from DNS data. The model was also validated for a higher Reynolds number of $Re_{\tau_o} \approx 395$ and showed very good agreements.

We showed that the liquid-infused surface (LIS) produces a meaningful amount of drag reduction in turbulent channel flow. Given the same groove geometry, the superhydrophobic surface (SHS) reduces more drag than LIS owing to much lower viscosity of air. However, LIS is more practical as it can maintain a stable lubricant–water interface under turbulent flows. In addition, owing to more stable interface for LIS (Rosenberg *et al.* 2016; Van Buren & Smits 2017), larger groove sizes of LIS can be used to achieve drag reduction comparable to that of the SHS. For example, a similar amount of drag reduction can be obtained with LIS when the groove width of the LIS (heptane) is twice that of the SHS.

Acknowledgements

This work was supported by the NRF programmes (2017M2A8A4018482 and 2016R1E1A1A02921549) of Ministry of Science and ICT, Korea.

REFERENCES

ALJALLIS, E., SARSHAR, M. A., DATLA, R., SIKKA, V., JONES, A. & CHOI, C.-H. 2013 Experimental study of skin friction drag reduction on superhydrophobic flat plates in high Reynolds number boundary layer flow. *Phys. Fluids* **25**, 025103.

BECHERT, D. W., BRUS, M., HAGE, W., VAN DER HOEVEN, J. G. T. & HOPPE, G. 1997 Experiment on drag-reduction surfaces and their optimization with an adjustable geometry. *J. Fluid Mech.* **338**, 59–87.

BELYAEV, A. V. & VINOGRADOVA, O. I. 2010 Effective slip in pressure-driven flow past super-hydrophobic stripes. *J. Fluid Mech.* **652**, 489–499.

BIDKAR, R. A., LEBLAC, L., KULKARNI, A. J., BAHADUR, V., CECCIO, S. L. & PERLIN, M. 2014 Skin-friction drag reduction in the turbulent regime using random-textured hydrophobic surfaces. *Phys. Fluids* **26**, 085108.

BUSSE, A. & SANDHAM, N. D. 2012 Influence of an anisotropic slip-length boundary condition on turbulent channel flow. *Phys. Fluids* **24**, 055111.

BUSSE, A., SANDHAM, N. D., MCHALE, G. & NEWTON, M. I. 2013 Change in drag, apparent slip and optimum air layer thickness for laminar flow over an idealised superhydrophobic surface. *J. Fluid Mech.* **727**, 488–508.

CARTAGENA, E. J. G., ARENAS, I., BERNARDINI, M. & LEONARDI, S. 2018 Dependence of the drag over super hydrophobic and liquid infused surfaces on the textured surface and Weber number. *Flow Turbul. Combust.* **100**, 945–960.

CHENG, Y. P., TEO, C. J. & KHOO, B. C. 2009 Microchannel flows with superhydrophobic surfaces: effects of Reynolds number and pattern width to channel height ratio. *Phys. Fluids* **21** (12), 122004.

CHOI, H., MOIN, P. & KIM, J. 1993 Direct numerical simulation of turbulent flow over riblets. *J. Fluid Mech.* **255**, 503.

COTTIN-BIZONNE, C., BARENTIN, C., CHARLAIX, É., BOCQUET, L. & BARRAT, J. L. 2004 Dynamics of simple liquids at heterogeneous surfaces: molecular-dynamics simulations and hydrodynamic description. *Eur. Phys. J.* E **15** (4), 427–438.

DANIELLO, R. J., WATERHOUSE, N. E. & ROTHSTEIN, J. P. 2009 Drag reduction in turbulent flows over superhydrophobic surfaces. *Phys. Fluids* **21**, 085103.

FAIRHALL, C. T. & GARCÍA-MAYORAL, R. 2018 Spectral analysis of the slip-length model for turbulence over textured superhydrophobic surfaces. *Flow Turbul. Combust.* **100**, 961–978.

FU, M. K., ARENAS, I., LEONARDI, S. & HULTMARK, M. 2017 Liquid-infused surfaces as a passive method of turbulent drag reduction. *J. Fluid Mech.* **824**, 688–700.

FUKAGATA, K., IWAMOTO, K. & KASAGI, N. 2002 Contribution of Reynolds stress distribution to the skin-friction in wall-bounded flows. *Phys. Fluids* **14**, L73–L76.

FUKAGATA, K., KASAGI, N. & KOUMOUTSAKOS, P. 2006 A theoretical prediction of friction drag reduction in turbulent flow by superhydrophobic surfaces. *Phys. Fluids* **18**, 051703.

GARCÍA-MAYORAL, R. & JIMÉNEZ, J. 2011 Drag reduction by riblets. *Phil. Trans. R. Soc. Lond.* A **369**, 1412–1427.

GE, Z., HOLMGREN, H., KRONBICHLER, M., BRANDT, L. & KREISS, G. 2018 Effective slip over partially filled microcavities and its possible failure. *Phys. Rev. Fluids* **3**, 054201.

GOLOVIN, K. B., GOSE, J. W., PERLIN, M., CECCIO, S. L. & TUTEJA, A. 2016 Bioinspired surfaces for turbulent drag reduction. *Phil. Trans. R. Soc. Lond.* A **374** (2073), 20160189.

GREIDANUS, A. J., DELFOS, R. & WESTERWEEL, J. 2011 Drag reduction by surface treatment in turbulent Taylor–Couette flow. *J. Phys.: Conf. Ser.* **318** (8), 082016.

HENOCH, C., KRUPENKIN, T., KOLODNER, P., TAYLOR, J., HODES, M., LYONS, A., PEGUERO, C. & BREUER, K. 2006 Turbulent drag reduction using superhydrophobic surfaces. In *Proceedings of the 3rd AIAA Flow Control Conference*, vol. 2, pp. 840–844. AIAA.

JELLY, T. O., JUNG, S. Y. & ZAKI, T. A. 2014 Turbulence and skin friction modification in channel flow with streamwise-aligned superhydrophobic surface texture. *Phys. Fluids* **26**, 095102.

JIMÉNEZ, J. 1994 On the structure and control of near wall turbulence. *Phys. Fluids* **6**, 944.

JIMÉNEZ, J. & MOIN, P. 1991 The minimal flow unit in near-wall turbulence. *J. Fluid Mech.* **225**, 213–240.

JUNG, T., CHOI, H. & KIM, J. 2016 Effects of the air layer of an idealized superhydrophobic surface on the slip length and skin-friction drag. *J. Fluid Mech.* **790**, R1.

JUNG, Y. C. & BHUSHAN, B. 2010 Biomimetic structures for fluid drag reduction in laminar and turbulent flows. *J. Phys.: Condens. Matter* **22**, 035104.

KIM, J., KIM, D. & CHOI, H. 2001 An immersed-boundary finite-volume method for simulations of flow in complex geometries. *J. Comput. Phys.* **171**, 132–150.

LAUGA, E. & STONE, H. 2003 Effective slip in pressure-driven Stokes flow. *J. Fluid Mech.* **489**, 55–77.

LEE, J., JELLY, T. O. & ZAKI, T. A. 2015 Effect of Reynolds number on turbulent drag reduction by superhydrophobic surface textures. *Flow Turbul. Combust.* **95**, 277–300.

LI, Y., ALAME, K. & MAHESH, K. 2017 Feature-resolved computational and analytical study of laminar drag reduction by superhydrophobic surfaces. *Phys. Rev. Fluids* **2** (5), 054002.

LING, H., SRINIVASAN, S., GOLOVIN, K., MCKINLEY, G. H., TUTEJA, A. & KATZ, J. 2016 High-resolution velocity measurement in the inner part of turbulent boundary layers over super-hydrophobic surfaces. *J. Fluid Mech.* **801**, 670–703.

LIU, Y., WEXLER, J. S., SCHÖNECKER, C. & STONE, H. A. 2016 Effect of viscosity ratio on the shear-driven failure of liquid-infused surfaces. *Phys. Rev. Fluids* **1** (7), 074003.

LUCHINI, P., MANZO, F. & POZZI, A. 1991 Resistance of a grooved surface to parallel flow and cross-flow. *J. Fluid. Mech.* **228**, 87–109.

MACDONALD, M., CHUNG, D., HUTCHINS, N., CHAN, L., OOI, A. & GARCÍA-MAYORAL, R. 2017 The minimal-span channel for rough-wall turbulent flows. *J. Fluid Mech.* **816**, 5–42.

MARTELL, M. B., PEROT, J. B. & ROTHSTEIN, J. P. 2009 Direct numerical simulations of turbulent flows over superhydrophobic surfaces. *J. Fluid Mech.* **620**, 31–41.

MARTELL, M. B., ROTHSTEIN, J. P. & PEROT, J. B. 2010 An analysis of superhydrophobic turbulent drag reduction mechanisms using direct numerical simulation. *Phys. Fluids* **22**, 065102.

MAYNES, D., JEFFS, K., WOOLFORD, B. & WEBB, B. W. 2007 Laminar flow in a microchannel with hydrophobic surface patterned microribs oriented parallel to the flow direction. *Phys. Fluids* **19**, 093603.

MIN, T. & KIM, J. 2004 Effects of hydrophobic surface on skin-friction drag. *Phys. Fluids* **16**, L55.

NIZKAYA, T. V., ASMOLOV, E. S. & VINOGRADOVA, O. I. 2014 Gas cushion model and hydrodynamic boundary condition for superhydrophobic textures. *Phys. Rev.* E **90**, 043017.

PARK, H., PARK, H. & KIM, J. 2013 A numerical study of the effects of superhydrophobic surface on skin-friction drag in turbulent channel flow. *Phys. Fluids* **25**, 110815.

PARK, H., SUN, G. & KIM, C.-J. C. 2014 Superhydrophobic turbulent drag reduction as a function of surface grating parameters. *J. Fluid Mech.* **747**, 722–734.

PEGUERO, C. & BREUER, K. 2009 On drag reduction in turbulent channel flow over superhydrophobic surfaces. In *Advance in Turbulence XII* (ed. B. Eckhardt), pp. 233–236. Springer.

RASTEGARI, A. & AKHAVAN, R. 2015 On the mechanism of turbulent drag reduction with superhydrophobic surfaces. *J. Fluid Mech.* **773**, R4.

RASTEGARI, A. & AKHAVAN, R. 2018 The common mechanism of turbulent skin-friction drag reduction with superhydrophobic longitudinal microgrooves and riblets. *J. Fluid Mech.* **838**, 68–104.

ROSENBERG, B. J., VAN BUREN, T., FU, M. K. & SMITS, A. J. 2016 Turbulent drag reduction over air- and liquid- impregnated surfaces. *Phys. Fluids* **28**, 015103.

ROTHSTEIN, J. P. 2010 Slip on superhydrophobic surfaces. *Annu. Rev. Fluid Mech.* **42**, 89–109.

SANGANI, A. S. & ACRIVOS, A. 1982 Slow flow through a periodic array of spheres. *Intl J. Multiphase Flow* **14** (4), 343–360.

SCHÖNECKER, C., BAIER, T. & HARDT, S. 2014 Influence of the enclosed fluid on the flow over a microstructured surface in the Cassie state. *J. Fluid Mech.* **740**, 168–195.

SCHÖNECKER, C. & HARDT, S. 2013 Longitudinal and transverse flow over a cavity containing a second immiscible fluid. *J. Fluid Mech.* **717**, 376–394.

SCHÖNECKER, C. & HARDT, S. 2015 Assessment of drag reduction at slippery, topographically structured surfaces. *Microfluid Nanofluid* **19**, 199–207.

SEO, J., GARCÍA-MAYORAL, R. & MANI, A. 2015 Pressure fluctuations and interfacial robustness in turbulent flows over superhydrophobic surfaces. *J. Fluid Mech.* **783**, 448–473.

SEO, J., GARCÍA-MAYORAL, R. & MANI, A. 2018 Turbulent flows over superhydrophobic surfaces: flow-induced capillary waves, and robustness of air-water interfaces. *J. Fluid Mech.* **835**, 45–85.

SEO, J. & MANI, A. 2016 On the scaling of the slip velocity in turbulent flows over superhydrophobic surfaces. *Phys. Fluids* **28**, 025110.

SOLOMON, B. R., KHALIL, K. S. & VARANASI, K. K. 2014 Drag reduction using lubricant-impregnated surfaces in viscous laminar flow. *Langmuir* **30** (36), 10970–10976.

SUN, R. & NG, C. O. 2017 Effective slip for flow through a channel bounded by lubricant-impregnated grooved surfaces. *Theor. Comput. Fluid Dyn.* **31** (2), 189–209.

TEO, C. J. & KHOO, B. C. 2009 Analysis of Stokes flow in microchannels with superhydrophobic surfaces containing a periodic array of micro-grooves. *Microfluid. Nanofluid.* **7**, 353–382.

TÜRK, S., DASCHIEL, G., STROH, A., HASEGAWA, Y. & FROHNAPFEL, B. 2014 Turbulent flow over superhydrophobic surfaces with streamwise grooves. *J. Fluid Mech.* **747**, 186–217.

VAN BUREN, T. & SMITS, A. J. 2017 Substantial drag reduction in turbulent flow using liquid-infused surfaces. *J. Fluid Mech.* **827**, 448–456.

VINOGRADOVA, O. I. 1995 Drainage of a thin liquid film confined between hydrophobic surfaces. *Langmuir* **11**, 2213–2220.

WALSH, M. J. 1983 Riblets as a viscous drag reduction technique. *AIAA J.* **21**, 485–486.

WEXLER, J. S., JACOBI, I. & STONE, H. A. 2015 Shear-driven failure of liquid-infused surfaces. *Phys. Rev. Lett.* **114** (16), 168301.

WONG, T. S., KANG, S. H., TANG, S. K., SMYTHE, E. J., HATTON, B. D., GRINTHAL, A. & AIZENBERG, J. 2011 Bioinspired self-repairing slippery surfaces with pressure-stable omniphobicity. *Nature* **477**, 443–447.

WOOLFORD, B., PRINCE, J., MAYNES, D. & WEBB, B. W. 2009 Particle image velocimetry characterization of turbulent channel flow with rib patterned superhydrophobic walls. *Phys. Fluids* **21**, 085106.

YBERT, C., BARENTIN, C., COTTIN-BIZONNE, C. C., JOSEPH, P. & BOCQUET, L. R. 2007 Achieving large slip with superhydrophobic surfaces: Scaling laws for generic geometries. *Phys. Fluids* **19**, 123601.

YOU, J., CHOI, H. & YOO, J. 2000 A modified fractional step method of keeping a constant mass flow rate in fully developed channel and pipe flows. *KSME Intl J.* **14** (5), 547–552.